A semi-analytical model of high-permittivity dielectric ring resonators for magnetic resonance imaging

Moussu, M.A.C.; Abdeddaim, R.; Dubois, M.; Georget, E.; Webb, A.G.; Nenasheva, E.; ... ; Enoch, S.

A Semi-Analytical Model of High-Permittivity Dielectric Ring Resonators for Magnetic Resonance Imaging

Marine A. C. Moussu, Redha Abdeddaim, Marc Dubois, Elodie Georget, Andrew G. Webb, *Member, IEEE*, Elizaveta Nenasheva, Pavel Belov, Stanislav Glybovski, *Member, IEEE*, Luisa Ciobanu, and Stefan Enoch

***Abstract*— Magnetic resonance imaging (MRI) is an imaging technique exploiting the magnetic resonance (MR) of specific nuclear spins, like protons. In this article, MR probes based on dielectric ring resonators are investigated from a theoretical approach. We take advantage of the high-permittivity and low-loss properties of the ceramic material used for manufacturing these probes for microscopy applications. Magnetic resonance microscopy (MRM) aims at imaging tiny samples with a sufficient resolution to distinguish small details. In this framework, compact resonators, called volume probes, contain the investigated sample and are used for both signal transmission and reception. The newly developed semi-analytical model enables the estimation of the frequency of the first transverse electric mode of a cylindrical resonator. It also provides a method to compute the corresponding magnetic field distribution, the dielectric losses contributions from the probe and the sample, and the signal-to-noise ratio (SNR). The proposed approach aims at providing design guidelines for dielectric probes.**

***Index Terms*— Dielectric resonators, magnetic resonance microscopy (MRM), signal-to-noise ratio (SNR), transverse electric mode.**

Manuscript received September 30, 2019; revised February 14, 2020; accepted February 23, 2020. Date of publication April 9, 2020; date of current version August 4, 2020. This work was supported in part by the European Union's Horizon 2020 Research and Innovation Program under Grant 736937 and in part by the Russian Foundation for Basic Research under Grant 18-32-20115. The work of Stanislav B. Glybovski was supported by the President of the Russian Federation under Grant MK-3620.2019.8. The work of Andrew G. Webb was supported in part by the H2020 European Research Council (ERC) Advanced Grant under Grant NOMA-MRI 670629. *(Corresponding author: Marine A. C. Moussu.)*

Marine A. C. Moussu is with Multiwave Imaging, 13013 Marseille, France, and also with Aix Marseille Univ, CNRS, Centrale Marseille, Institut Fresnel, 13013 Marseille, France (e-mail: marine.moussu@fresnel.fr).

Redha Abdeddaim is with Aix Marseille Univ, CNRS, Centrale Marseille, Institut Fresnel, 13013 Marseille, France (e-mail: redha.abdeddaim@fresnel.fr).

Marc Dubois is with Aix Marseille Univ, CNRS, Center for Magnetic Resonance in Biology and Medicine, 13005 Marseille, France, and also with Aix Marseille Univ, CNRS, Centrale Marseille, Institut Fresnel, 13013 Marseille, France (e-mail: marc.dubois@fresnel.fr).

Elodie Georget is with Multiwave Imaging, 13013 Marseille, France (e-mail: elodie@multiwaveimaging.com).

Andrew G. Webb is with the Department of Radiology, C.J. Gorter Center for High Field MRI, Leiden University Medical Center, 2333 ZA Leiden, The Netherlands (e-mail: a.webb@lumc.nl).

Elizaveta Nenasheva is with Ceramics Co. Ltd., 194223 Saint Petersburg, Russia (e-mail: liza@ceramics.sp.ru).

Pavel Belov and Stanislav Glybovski are with ITMO University, 197101 Saint Petersburg, Russia (e-mail: belov@metalab.ifmo.ru; s.glybovski@metalab.ifmo.ru).

Luisa Ciobanu is with the Commissariat à l'Energie Atomique et aux Energies Alternatives (CEA), Direction de la Recherche Fondamentale (DRF), Institut des Sciences du Vivant Frédéric-Joliot (JOLIOT), NeuroSpin, Université Paris-Saclay, Gif-sur-Yvette, France (e-mail: luisa.ciobanu@cea.fr).

Stefan Enoch is with Aix Marseille Univ, CNRS, Centrale Marseille, Institut Fresnel, Institut Marseille Imaging, 13013 Marseille, France (e-mail: stefan.enoch@fresnel.fr).

Color versions of one or more of the figures in this article are available online at http://ieeexplore.ieee.org.

Digital Object Identifier 10.1109/TAP.2020.2980771

I. Introduction

MAGNETIC resonance microscopy (MRM) is an imaging technique that uses the principles of magnetic resonance imaging (MRI) to produce images with a spatial resolution of less than 100 μm on at least one of the three dimensions [1]. Typical sample sizes are several millimeters or less, which places high demands on achieving the optimum signal-to-noise ratio (SNR). For these reasons, MRM is usually performed using magnets with a static field B_0 of more than 7 T and up to 22 T, which is currently the strongest available magnet for imaging [1]. At such an ultrahigh magnetic field, the reference probe for volume imaging is often a solenoid, with diameter closely matching that of the sample. The solenoid produces a large, homogeneous radio-frequency (RF) field B_1 used for excitation but also a high electric field that can produce heating due to resistive losses in the conductive samples [2]. Researchers have recently introduced configurations based on ceramic dielectric resonators to reduce contribution to the noise due to the electric field in the sample [3]–[5].

These resonators have been successively introduced in microwave engineering. They are used to reduce significantly the size of the microwave circuits, especially in the evergrowing field of telecommunications [6]. They are exploited as antennas (TE mode with high-quality factor) [7]–[9] and filters (hybrid electric and magnetic (HEM) mode with low Q-factor) [9]–[11]. Electron paramagnetic resonance (EPR) is another application of such resonators to concentrate the magnetic field into a specific region [3].

In MRM, to compete with the solenoid coil, the first transverse electric mode of a cylindrical dielectric cavity, the so-called $TE_{01\delta}$, is employed as it has a maximum axial magnetic field in its center together with a minimum of the electric field [6]. Fig. 1 shows the placement of this probe within the bore of an MRI magnet. In this position, the orthogonality of B_1 and B_0 needed for spins excitation and signal detection is guaranteed by the axial direction of the main B_1 component related to this mode. Several prototypes of such ceramic rings

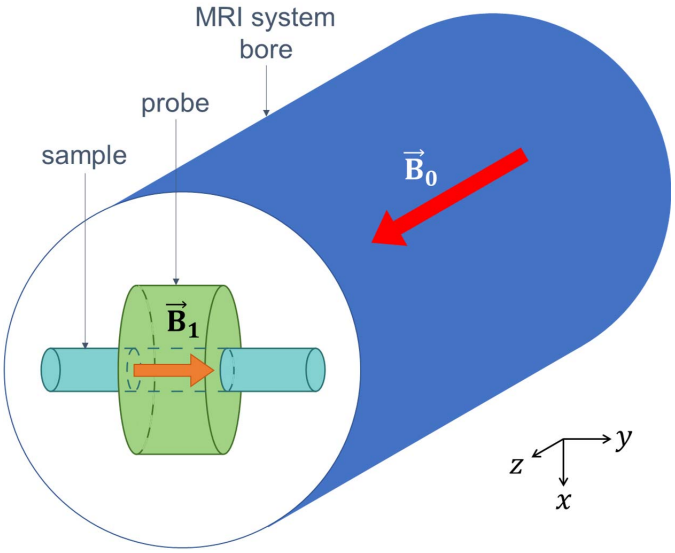

Fig. 1. Configuration of the setup: the axis of the dielectric probe is perpendicular to the MRI system axis.

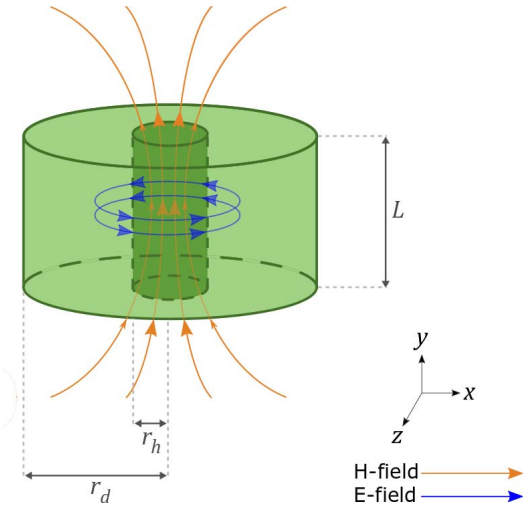

Fig. 2. $TE_{01\delta}$ mode of a ring resonator (schematic field lines), notations, and coordinate system.

were experimentally compared with a commercial reference probe and provided an equivalent or higher SNR [4], [5].

While the theoretical model for solenoid coils used as MR probes has been well developed [12], [13], no detailed theoretical model was so far proposed for MR probes based on dielectric ring resonators. However, such a model could give the possibility of adjusting the ceramics properties and resonator dimensions to design dielectric probes with maximum efficiency for a given sample.

The resonant frequencies, the field distribution, and the quality factor of cylindrical dielectric resonators have been investigated for many years. From the literature, two types of approaches can be distinguished.

1) Accurate and rigorous methods with high computational cost, allowing determining both the resonant frequencies and the field distribution while considering complex configurations (shielded dielectric resonator, in a waveguide, isolated, on a substrate, and so on). Among others, these methods are the surface integral inteqation solved with the method of moments [14], the perturbational approach with asymptotic expansions [15], [16], the finite-element method [17], and the mode-matching methods for solving the corresponding boundary value problem [6], [10], [11].
2) Simplified models that provide an approximated estimation of the characteristics of a given mode, most of the time the first TE or TM mode.
    a) Perfect magnetic conductor (PMC) walls are assumed at the lateral boundaries of the resonator like in [18] and [8], or second-order Cohn's model for both isolated and shielded resonators [19].
    b) The tangential field continuity is ensured at the resonator lateral boundaries and/or at its terminal ends like in Itoh and Rudoka's model [20].

More recently, such an approximated theoretical model of a cylindrical dielectric resonator's first TE mode, based on the lumped-element equivalent circuit approach, has been developed for EPR applications [21], [22].

In this article, we present a model describing the excited field distribution of ceramic probe: the first transverse electric mode ($TE_{01\delta}$) of a cylindrical, high-permittivity resonator. Our model is described as "semi-analytical" in the following, because it is based on the analytical expression of the electromagnetic (EM) field but requires the numerical solving of a set of equations to estimate the wavenumbers describing the field. In this approach, the ceramic probe consists of a dielectric ring (green on Fig. 1) containing a sample medium (light blue). A formula is proposed for the resonant frequency of this system, which is approximated to that of a filled disk, assuming that the effect of the hole is negligible for the frequency. The field distribution is computed from the description of the EM field in the sample, within the dielectric ring, and around it. This semi-analytical approach is then used to derive a quantitative estimation of the reachable SNR performance of ceramic probes. The practical example used is designed for a Larmor frequency $f_L = 730$ MHz and previously presented experimentally in [23], with a ring of a given height of 10 mm, outer diameter 18 mm, and inner diameter 5.6 mm, and a dielectric material of relative permittivity 536 and loss tangent 8×10^{-4}.

II. $TE_{01\delta}$ Mode Description

The principle of the dielectric probe presented in this article relies on the excitation of its first TE mode, where the magnetic field distribution in the sample is similar to that of the solenoid coil, while its electric field spatial behavior is radically different. In this section, we provide semi-analytic tools to describe the EM field of the exploited $TE_{01\delta}$, in order to, in Section III, derive an expression for the dielectric losses induced by this probe.

The ceramic probe is a cylindrical ring resonator, as shown in Fig. 2, made of a material with a very high permittivity (to ensure a good mode confinement), low-loss (to lower the probe intrinsic losses) dielectric material surrounded by a low-permittivity medium (air). Due to the high-permittivity

contrast between the background material and the resonator, the EM-field distribution at resonance can be assumed to be mainly confined within the resonator. The reflection coefficient between the air and the high-permittivity dielectric material, equal to $(\sqrt{\epsilon_r}-1)/(\sqrt{\epsilon_r}+1)$ [24], is indeed close to 1. In this context, the first analytical approaches of cylindrical dielectric resonators are based on the assumption of PMC boundary conditions at the lateral frontiers of the structure [18], [25].

The resonant modes of such a cylindrical structure are classified following the same notations as of the metallic cavities, except that the integer numbers quantifying the wavenumbers are replaced by noninteger numbers [26]. In cylindrical coordinates (ρ, θ, y), a transverse electric mode is fully described by its axial magnetic component H_y, whose generic expression within the cavity is given for a disk resonator in Eq. (1) [25], [27]

$$\mathrm{H}_y = A\cos(n\theta+\phi)\mathrm{J}_n(\alpha\rho)\cos(\beta y+\psi). \tag{1}$$

The mode nomenclature for a dielectric cavity is of the form $\mathrm{TE}_{nm(p+\delta)}$ in reference to the metallic cavities, where n is the integer number of the field angular variations, m an integer number describing the order of the radial field variations, and $p+\delta$ (p integer, δ a number between 0 and 1) quantifying the product βL of the axial wavenumber β with the resonator height L. The first transverse electric mode of a cylindrical resonator, named $\mathrm{TE}_{01\delta}$, corresponds to an EM field with a cylindrical symmetry with respect to the resonator axis (no angular variation). In the center, the electric field **E** decreases to zero, while the magnetic field **H** is maximum and mainly parallel to the resonator axis [3], [6], two features of great interest for an MRM probe.

A. Disk Resonator Frequency Estimation

In this section, several approaches for estimating the $\mathrm{TE}_{01\delta}$ mode eigenfrequency of a cylindrical dielectric resonator, neglecting the dielectric losses within the resonator material, are presented. In the microwave resonator literature, one can find a wide variety of methods developed to estimate the $\mathrm{TE}_{01\delta}$ mode frequency with different levels of accuracy. A first starting point is to approximate the value of the resonant frequency of the isolated resonator by (2) [6], with f_{MHz} the frequency in megahertz, ϵ_r the relative permittivity, r_d the disk radius, and L the disk height. This equation was deduced by fitting simulation data, and despite a limited domain of validity (radius over height ratio: $0.5 < r_\mathrm{d}/L < 2$ and relative permittivity: $30 < \epsilon_\mathrm{r} < 50$) where accuracy is ensured around 2%, it can be used to give a reasonable approximation for any high-permittivity disk resonator

$$f_{\mathrm{MHz}} = \frac{3400}{\sqrt{\epsilon_\mathrm{r}} r_{\mathrm{d,cm}}}\left(\frac{r_\mathrm{d}}{L}+3.45\right). \tag{2}$$

To extend the validity range of the estimation in terms of resonator parameters, the simplest approach in terms of computational cost consists in considering the cylindrical dielectric resonator as a shortened section of an infinite dielectric waveguide with no field leakages on its lateral boundaries. The radial wavenumber α is the same as for a circular waveguide with PMC lateral boundaries $\alpha = (x_{01}/r_d)$, where x_{01} is the first zero of the Bessel function of the first kind, of order zero, and r_d the cylinder radius [19]. The axial wavenumbers ($\beta^2 = \epsilon_r k_0^2 - \alpha^2$ within the dielectric and $\gamma^2 = k_0^2 - \alpha^2$ outside, and k_0 the wavenumber in vacuum) are related to the resonant frequency $f_{\mathrm{cutoff}} = k_0 c_0/(2\pi)$ (with c_0 the speed of light in vacuum) through the transcendental equation $\beta\tan(\beta L/2) = \gamma$, as covered in [25] under the description of the cutoff waveguide approach. This method usually underestimates the resonant frequency of the first TE mode [20].

An empirical formula was also proposed in [28] and [29] to provide a reliable estimation of the resonant frequency $f_{\mathrm{empirical}}$

$$f_{\mathrm{empirical}} = \frac{2.9c}{2\pi r_\mathrm{d}\epsilon_\mathrm{r}^{0.46}}\left[0.7+0.3\frac{r_\mathrm{d}}{L}-0.03\left(\frac{r_\mathrm{d}}{L}\right)^2\right]. \tag{3}$$

Similar to the method presented in [30], the resonant frequency f_{res} is estimated as the average of the two last approaches, as expressed in

$$f_{\mathrm{res}} = \frac{1}{2}\left(f_{\mathrm{empirical}} + f_{\mathrm{cutoff}}\right). \tag{4}$$

For comparison with a reference method, the gold-standard resonance frequency of the same dielectric disk $f_{\mathrm{ref,disk}}$ is calculated using the numerical simulations with the Eigenmode Solver of CST Microwave Studio. The reliability of the proposed method that provides the approximated value f_{res} (4) was investigated by comparison with the numerical simulations for discretized values among the following parameter ranges:

1) relative permittivity ϵ_r varying from 200 to 1000;
2) disk height L from 5 to 20 mm;
3) disk radius r_d from 5 to 15 mm.

In Fig. 3, the resonant frequency is calculated using (4) for a continuous range of height, and discrete values of the disk radius and relative permittivity. The comparison of these results with the gold standard is quantified through the relative error defined in (5). For the considered ranges of parameters, the proposed estimation f_{res} has a maximum relative error of 5.3%; all other cases have an error less than 5% and more than half are below 3%, which validates this approach

$$\mathcal{E}_{f,\mathrm{ref}} = \frac{|f_{\mathrm{res}} - f_{\mathrm{ref,disk}}|}{f_{\mathrm{ref,disk}}} \times 100. \tag{5}$$

The MRM ceramic probe studied is described as a high-permittivity ($\epsilon_d = \epsilon_0\epsilon_r$) ring resonator (outer radius r_d, inner radius r_h, and height L), filled with a lower permittivity (ϵ_s) material representing the sample (cylinder of radius r_h and height L). Such a structure has resonant modes that can be described in the same manner as for a disk of the same high-permittivity ϵ_r than the probe [17]. In the particular case of the first TE mode, equating the field distribution of the probe and the disk resonators is even a reasonable assumption. Indeed, the first TE-mode features are affected in proportion to the electric and magnetic energies stored in the involved volume [31], which coarsely depends on the quantity $\Delta\epsilon \times \mathrm{V}_{\mathrm{samp}}$ ($\Delta\epsilon = \epsilon_\mathrm{s} - \epsilon_\mathrm{d}$ and $\mathrm{V}_{\mathrm{samp}}$ the sample volume). In particular, at first approximation, the mode frequency varies from the value f_{disk} of the disk to f_{probe} for the probe according

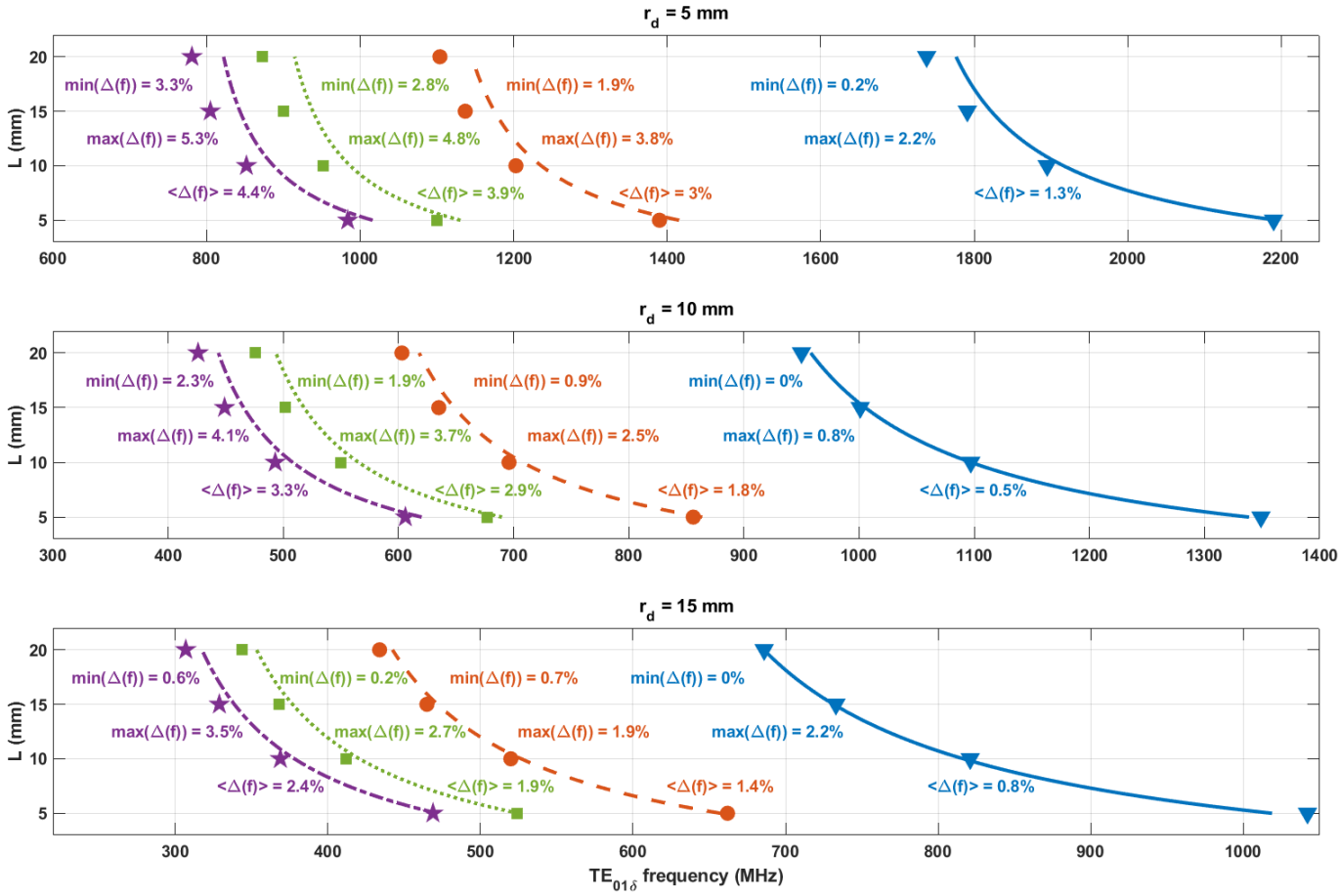

Fig. 3. Comparison between the numerical simulations and the semi-analytical method [see (4)] of $TE_{01\delta}$ eigenmode frequency estimation as a function of the disk height (L), radius (r_d), and permittivity (blue: 200; orange: 500; green: 800; purple: 1000). Lines represent the results of the semi-analytical method proposed in this article [f_{res}; see (4)], and markers represent the CST results. For each curve, the maximum, minimum, and averaged values of the relative error Δ(f) are indicated.

to (6) from [31].

$$\frac{f_{\text{probe}} - f_{\text{disk}}}{f_{\text{disk}}} \approx \frac{-\iiint_{V_{\text{samp}}} \Delta\epsilon |\vec{E}_{\text{disk}}|^2 d^3\mathbf{r}}{\iiint_{V_{\text{ring}} \cup V_{\text{samp}}} \left(\epsilon_{\text{d}} |\vec{E}_{\text{disk}}|^2 + \mu_0 |\vec{H}_{\text{disk}}|^2\right) d^3\mathbf{r}}. \tag{6}$$

From this expression, it can be seen that the TE-mode frequency is affected by the permittivity contrast between the dielectric ring and the sample. More precisely, as the sample has a lower permittivity than the ring material, the permittivity contrast $\Delta\epsilon$ is negative and the frequency shift is, therefore, positive. In the framework of MRI, it means that the working frequency of the dielectric probe depends on the sample, and therefore must be adjusted on demand at the desired nucleus Larmor frequency. To do so, several methods have been developed, including coupling with copper foils [4] or with a second dielectric resonator [5], and thermostating the probe to change its permittivity as it depends on the temperature [23]. On the other side, the sample volume V_{samp} is in the region where the E-field distribution is minimum, as it vanishes in the center of the structure. In this article, we assume the same field distribution for the system {ring + sample} as for the disk when estimating the mode frequency in this section and the SNR factor in Section IV. This hypothesis is valid, while the permittivity contrast, together with the sample over the disk radii ratio $r_{\text{h}}/r_{\text{d}}$, have reasonable values, as presented in the following.

Fig. 4 shows the influence of the sample on the $TE_{01\delta}$ mode frequency in the case of a probe with outer radius $r_{\text{d}} = 10$ mm, height $L = 10$ mm, and varying permittivity ϵ_{r} and sample properties r_{h} and $\epsilon_{\text{r,samp}}$. The frequencies used in this part are estimated with the Eigenmode Solver of CST Studio. For three values of the relative permittivity of the dielectric material constituting the probe ϵ_{r} (200, 500, and 800), the relative variation $\mathcal{E}_{f,\text{disk/probe}}$ between the disk frequency $f_{\text{ref,disk}}$ and the probe one $f_{\text{ref,probe}}$ is estimated:

$$\mathcal{E}_{f,\text{disk/probe}} = \frac{|f_{\text{ref,probe}} - f_{\text{ref,disk}}|}{f_{\text{ref,disk}}} \times 100. \tag{7}$$

The sample permittivity range covers a wide variety of biological samples. As expected from (6), the relative variation is a linear function of the sample permittivity. A general observation from this figure is that the radii ratio $r_{\text{h}}/r_{\text{d}}$ has a dominant influence over the frequency variation (all the more that the relative permittivity of the probe ring is high). Indeed, while the sample radius r_{h} is smaller than 0.4 times the probe radius r_{d}, the frequency shift due to the sample is inferior to 5% for all the considered permittivities.

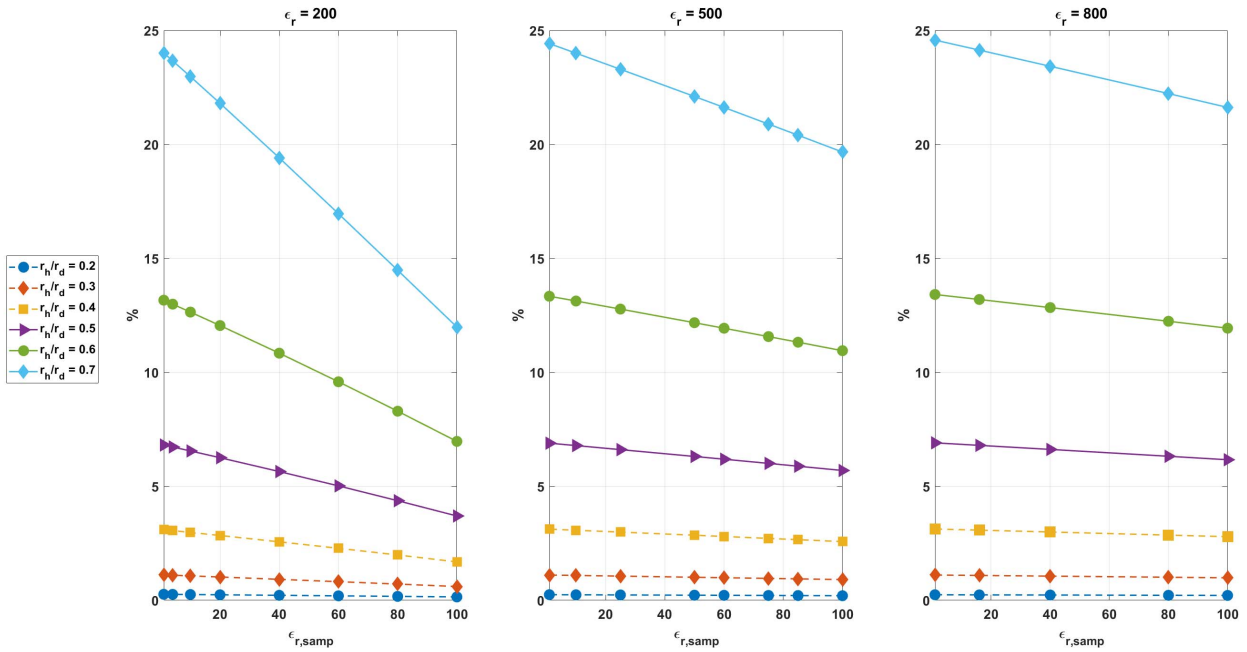

Fig. 4. Quantification of the $TE_{01\delta}$ mode frequency shift between the disk resonator and the dielectric probe (for both, numerical simulation results with CST Eigenmode Solver). The probe ring has its relative permittivity equal to 200 (left), 500 (center), and 800 (right). The frequency variation is plotted as a function of the sample permittivity and for several discrete values of the radii ratio. Curves in dashed lines correspond to systematic frequency shift inferior to 5%.

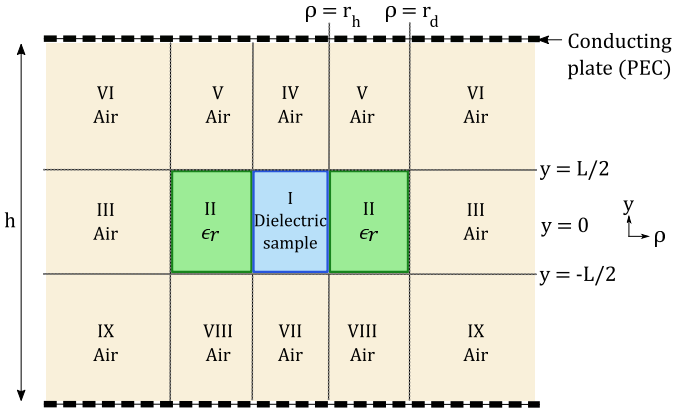

Fig. 5. Part-by-part space subdivision for field estimation.

B. Field Distribution

As for the resonance frequency of the $TE_{01\delta}$ mode of a disk resonator, several approaches have been proposed to estimate the corresponding EM-field distribution: rigorous numerical methods with heavy computation cost and simplified models, in which error depends on the rudeness of the hypothesis [6]. Among the second category, the approach proposed by Sheen [32] is an interesting tradeoff between the accuracy of the field distribution and the simplicity of implementation. In [32], it is presented for the parallel-plate dielectric disk, meaning the disk is placed between two conducting plates. In the following, we propose a similar method for the parallel-plate dielectric ring. In both methods, the field distribution is estimated for lossless dielectric materials.

This method, for computing the field distribution of the ring-resonator $TE_{01\delta}$ mode, is based on the part-by-part subdivision of the space surrounding the resonator. These regions are indexed from I $\rightarrow$ IX and are shown in Fig. 5. Each of these regions corresponds to a homogeneous relative permittivity distribution: region I represents the sample, region II the ceramic material constitutive of the probe, and regions III $\rightarrow$ IX the surrounding media that are here taken as air ($\epsilon_{r,\mathrm{III}\rightarrow\mathrm{IX}} = 1$).

The next step consists in analytically describing the mode in a cylindrical coordinate system (ρ, θ, y). According to its specifications, this TE mode has a cylindrical symmetry, which means that only three field components are nonzero [6], [27]: H_y, E_θ, and H_ρ. Solving Helmholtz's equation in cylindrical coordinates leads to the following field expression properties [6].

1) The radial variation involves the linear combinations of the Bessel functions J and Y or the modified Bessel function K, with the radial wavenumber $k_{\rho,i}$ in region i.
2) The axial variation is expressed with a sinusoidal function and the axial wavenumber $k_{y,i}$ in region i.

The wavenumber components in region i are related to the total wavenumber in vacuum k_0 by

$$k_{\rho,i}^2 + k_{y,i}^2 = \epsilon_{r,i} k_0^2. \tag{8}$$

The model is based on the assumption of purely propagative EM field in the probe, with real wavenumbers $k_{\rho,II} = \alpha_{\mathrm{II}}$ and $k_{y,II} = \beta$ in the dielectric ring, that imposes the mode. Leakages through the resonator boundaries are also considered. In the sample (region I), the axial wavenumber is real by field continuity with the ring, but the radial wavenumber α_{I} is defined by the relative values of k_0 and $k_{\rho,\mathrm{II}}$. Outside the probe, the field is either propagative or evanescent in one or two directions, y and ρ. For evanescent contributions, the corresponding wavenumber is imaginary: $k_{\rho,\mathrm{i}} = j\nu_{\mathrm{i}}$ and $k_{\mathrm{y,i}} = j\gamma_{\mathrm{i}}$.

The field expressions for H_y and E_θ are given in (9) and (10), respectively. The third component H_ρ can be derived from H_y, and its expression is provided in regions I, IV, and VII [see (11)] only since the others are unused in the following for calculations:

$$\begin{aligned}
H_y^{\mathrm{I}} &= a_{\mathrm{I}} J_0(\alpha_{\mathrm{I}}\rho)\cos(\beta y)\\
H_y^{\mathrm{II}} &= a_{\mathrm{II}}[J_0(\alpha_{\mathrm{II}}\rho)+\xi Y_0(\alpha_{\mathrm{II}}\rho)]\cos(\beta y)\\
H_y^{\mathrm{III}} &= a_{\mathrm{III}} K_0(\nu_{\mathrm{III}}\rho)\cos(\beta y)\\
H_y^{\mathrm{IV}} &= a_{\mathrm{IV}} J_0(\alpha_{\mathrm{I}}\rho)\sinh[\gamma\,(y-y_{\mathrm{lim}})]\\
H_y^{\mathrm{V}} &= a_{\mathrm{V}}[J_0(\alpha_{\mathrm{II}}\rho)+\xi Y_0(\alpha_{\mathrm{II}}\rho)]\sinh[\gamma\,(y-y_{\mathrm{lim}})]\\
H_y^{\mathrm{VI}} &= a_{\mathrm{VI}} K_0(\nu_{\mathrm{III}}\rho)\sinh[\gamma\,(y-y_{\mathrm{lim}})]\\
H_y^{\mathrm{VII}} &= a_{\mathrm{VII}} J_0(\alpha_{\mathrm{I}}\rho)\sinh[-\gamma\,(y+y_{\mathrm{lim}})]\\
H_y^{\mathrm{VIII}} &= a_{\mathrm{VIII}}[J_0(\alpha_{\mathrm{II}}\rho)+\xi Y_0(\alpha_{\mathrm{II}}\rho)]\sinh[-\gamma\,(y+y_{\mathrm{lim}})]\\
H_y^{\mathrm{IX}} &= a_{\mathrm{IX}} K_0(\nu_{\mathrm{III}}\rho)\sinh[-\gamma\,(y+y_{\mathrm{lim}})] \qquad (9)\\
E_\theta^{\mathrm{I}} &= a_{\mathrm{I}}\frac{j\omega\mu_0}{\alpha_{\mathrm{I}}} J_1(\alpha_{\mathrm{I}}\rho)\cos(\beta y)\\
E_\theta^{\mathrm{II}} &= a_{\mathrm{II}}\frac{j\omega\mu_0}{\alpha_{\mathrm{II}}}[J_1(\alpha_{\mathrm{II}}\rho)+\xi Y_1(\alpha_{\mathrm{II}}\rho)]\cos(\beta y)\\
E_\theta^{\mathrm{III}} &= -a_{\mathrm{III}}\frac{j\omega\mu_0}{\nu_{\mathrm{III}}} K_1(\nu_{\mathrm{III}}\rho)\cos(\beta y)\\
E_\theta^{\mathrm{IV}} &= a_{\mathrm{IV}}\frac{j\omega\mu_0}{\alpha_{\mathrm{I}}} J_1(\alpha_{\mathrm{I}}\rho)\sinh[\gamma\,(y-y_{\mathrm{lim}})]\\
E_\theta^{\mathrm{V}} &= a_{\mathrm{V}}\frac{j\omega\mu_0}{\alpha_{\mathrm{II}}}[J_1(\alpha_{\mathrm{II}}\rho)+\xi Y_1(\alpha_{\mathrm{II}}\rho)]\\
&\quad\times\sinh[\gamma\,(y-y_{\mathrm{lim}})]\\
E_\theta^{\mathrm{VI}} &= -a_{\mathrm{VI}}\frac{j\omega\mu_0}{\nu_{\mathrm{III}}} K_1(\nu_{\mathrm{III}}\rho)\sinh[\gamma\,(y-y_{\mathrm{lim}})]\\
E_\theta^{\mathrm{VII}} &= a_{\mathrm{VII}}\frac{j\omega\mu_0}{\alpha_{\mathrm{I}}} J_1(\alpha_{\mathrm{I}}\rho)\sinh[-\gamma\,(y+y_{\mathrm{lim}})]\\
E_\theta^{\mathrm{VIII}} &= a_{\mathrm{VIII}}\frac{j\omega\mu_0}{\alpha_{\mathrm{II}}}[J_1(\alpha_{\mathrm{II}}\rho)+\xi Y_1(\alpha_{\mathrm{II}}\rho)]\\
&\quad\times\sinh[-\gamma\,(y+y_{\mathrm{lim}})]\\
E_\theta^{\mathrm{IX}} &= -a_{\mathrm{IX}}\frac{j\omega\mu_0}{\nu_{\mathrm{III}}} K_1(\nu_{\mathrm{III}}\rho)\sinh[-\gamma\,(y+y_{\mathrm{lim}})] \qquad (10)\\
H_\rho^{\mathrm{I}} &= -a_{\mathrm{I}}\frac{\beta}{\alpha_{\mathrm{I}}} J_1(\alpha_{\mathrm{I}}\rho)\sin(\beta y)\\
H_\rho^{\mathrm{IV}} &= a_{\mathrm{IV}}\frac{\gamma}{\alpha_{\mathrm{I}}} J_1(\alpha_{\mathrm{I}}\rho)\cosh[\gamma\,(y-y_{\mathrm{lim}})]\\
H_\rho^{\mathrm{VII}} &= -a_{\mathrm{VII}}\frac{\gamma}{\alpha_{\mathrm{I}}} J_1(\alpha_{\mathrm{I}}\rho)\cosh[-\gamma\,(y+y_{\mathrm{lim}})]. \qquad (11)
\end{aligned}$$

The axial wavenumber γ is the same in absolute value be it for $y > (L/2)$ (regions IV–VI) or $y < -(L/2)$ (regions VII–IX), since the resonator is at equal distance from the conducting plates. The E-field cancellation on the PEC boundaries gives $y_{\mathrm{lim}} = (h/2)$. In the following examples, h is taken equal to 11 cm, which corresponds to the shielded bore diameter of the MRI device used in [23].

The wavenumber components are determined using the tangential field continuity conditions in (12): $H_y^{\mathrm{I}} = H_y^{\mathrm{II}}$ and $E_\theta^{\mathrm{I}} = E_\theta^{\mathrm{II}}$ at $\rho = r_{\mathrm{h}}$, $H_y^{\mathrm{II}} = H_y^{\mathrm{III}}$, and $E_\theta^{\mathrm{II}} = E_\theta^{\mathrm{III}}$ at $\rho = r_{\mathrm{d}}$, and $E_\theta^{\mathrm{I}} = E_\theta^{\mathrm{IV}}$ and $H_y^{\mathrm{I}} = H_y^{\mathrm{IV}}$ at $y = \pm\frac{L}{2}$. The latest is written only at $y = +\frac{L}{2}$, as it gives the same equation

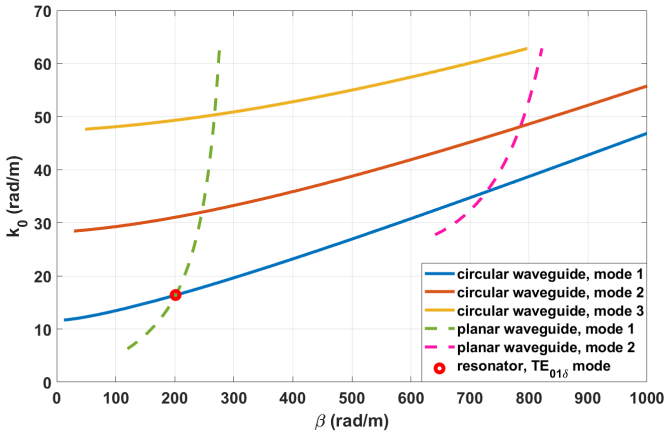

Fig. 6. Dispersion curves of the infinite dielectric circular (solid lines) and planar (dashed lines) waveguides corresponding to the cylindrical resonator from [23] (with $\epsilon_{\mathrm{r,samp}} = 50$). Only the three (respectively, two) first modes of the circular (respectively, planar) waveguide can be seen in the considered ranges of frequencies and β values. The first TE mode of this ring resonator is shown with a red circle at the intersection point of the first waveguides modes.

compared to $y = -\frac{L}{2}$

$$\begin{aligned}
a_{\mathrm{I}} J_0(\alpha_{\mathrm{I}} r_{\mathrm{h}}) &= a_{\mathrm{II}}[J_0(\alpha_{\mathrm{II}} r_{\mathrm{h}})+\xi Y_0(\alpha_{\mathrm{II}} r_{\mathrm{h}})]\\
\frac{a_{\mathrm{I}}}{\alpha_{\mathrm{I}}} J_1(\alpha_{\mathrm{I}} r_{\mathrm{h}}) &= \frac{a_{\mathrm{II}}}{\alpha_{\mathrm{II}}}[J_1(\alpha_{\mathrm{II}} r_{\mathrm{h}})+\xi Y_1(\alpha_{\mathrm{II}} r_{\mathrm{h}})]\\
a_{\mathrm{II}}[J_0(\alpha_{\mathrm{II}} r_{\mathrm{d}})+\xi Y_0(\alpha_{\mathrm{II}} r_{\mathrm{d}})] &= a_{\mathrm{III}} K_0(\nu_{\mathrm{III}} r_{\mathrm{d}})\\
\frac{a_{\mathrm{II}}}{\alpha_{\mathrm{II}}}[J_1(\alpha_{\mathrm{II}} r_{\mathrm{d}})+\xi Y_1(\alpha_{\mathrm{II}} r_{\mathrm{d}})] &= -\frac{a_{\mathrm{III}}}{\nu_{\mathrm{III}}} K_1(\nu_{\mathrm{III}} r_{\mathrm{d}})\\
a_{\mathrm{I}}\cos\left(\frac{\beta L}{2}\right) &= a_{\mathrm{IV}}\sinh\left(\gamma\,\frac{L-h}{2}\right)\\
-a_{\mathrm{I}}\beta\sin\left(\frac{\beta L}{2}\right) &= a_{\mathrm{IV}}\gamma\cosh\left(\gamma\,\frac{L-h}{2}\right). \qquad (12)
\end{aligned}$$

Combining the first four equations of (12) and (8) leads to the set of equations (13), which is equivalent to the eigenvalue problem of a circular dielectric waveguide, as presented in [33]. This type of system of equations admits complex solutions, as demonstrated in [34]. It is numerically solved with respect to the real variable β. The solutions of this system can be graphically represented by distinct curves representing the wavenumber k_0 as a function of β. The dispersion curves of the first three modes of such a waveguide are shown as an example in Fig. 6. The lowest frequency curve is the first-order mode of the corresponding infinite dielectric waveguide and is the solution considered in the following:

$$\begin{aligned}
\frac{J_1(u)}{uJ_0(u)} &= \frac{1}{v}\frac{J_1(v)+\xi Y_1(v)}{J_0(v)+\xi Y_0(v)}\\
-\frac{K_1(x)}{xK_0(x)} &= \frac{1}{\frac{r_{\mathrm{d}}}{r_{\mathrm{h}}}v}\frac{J_1\left(\frac{r_{\mathrm{d}}}{r_{\mathrm{h}}}v\right)+\xi Y_1\left(\frac{r_{\mathrm{d}}}{r_{\mathrm{h}}}v\right)}{J_0\left(\frac{r_{\mathrm{d}}}{r_{\mathrm{h}}}v\right)+\xi Y_0\left(\frac{r_{\mathrm{d}}}{r_{\mathrm{h}}}v\right)}\\
u &= r_{\mathrm{h}}\sqrt{\epsilon_{r,samp}k_0^2-\beta^2}\\
v &= r_{\mathrm{h}}\sqrt{\epsilon_r k_0^2-\beta^2}\\
x &= r_{\mathrm{d}}\sqrt{-k_0^2+\beta^2}\\
\xi &= \frac{uJ_0(u)J_1(v)-vJ_0(v)J_1(u)}{vY_0(v)J_1(u)-uJ_0(u)Y_1(v)}. \qquad (13)
\end{aligned}$$

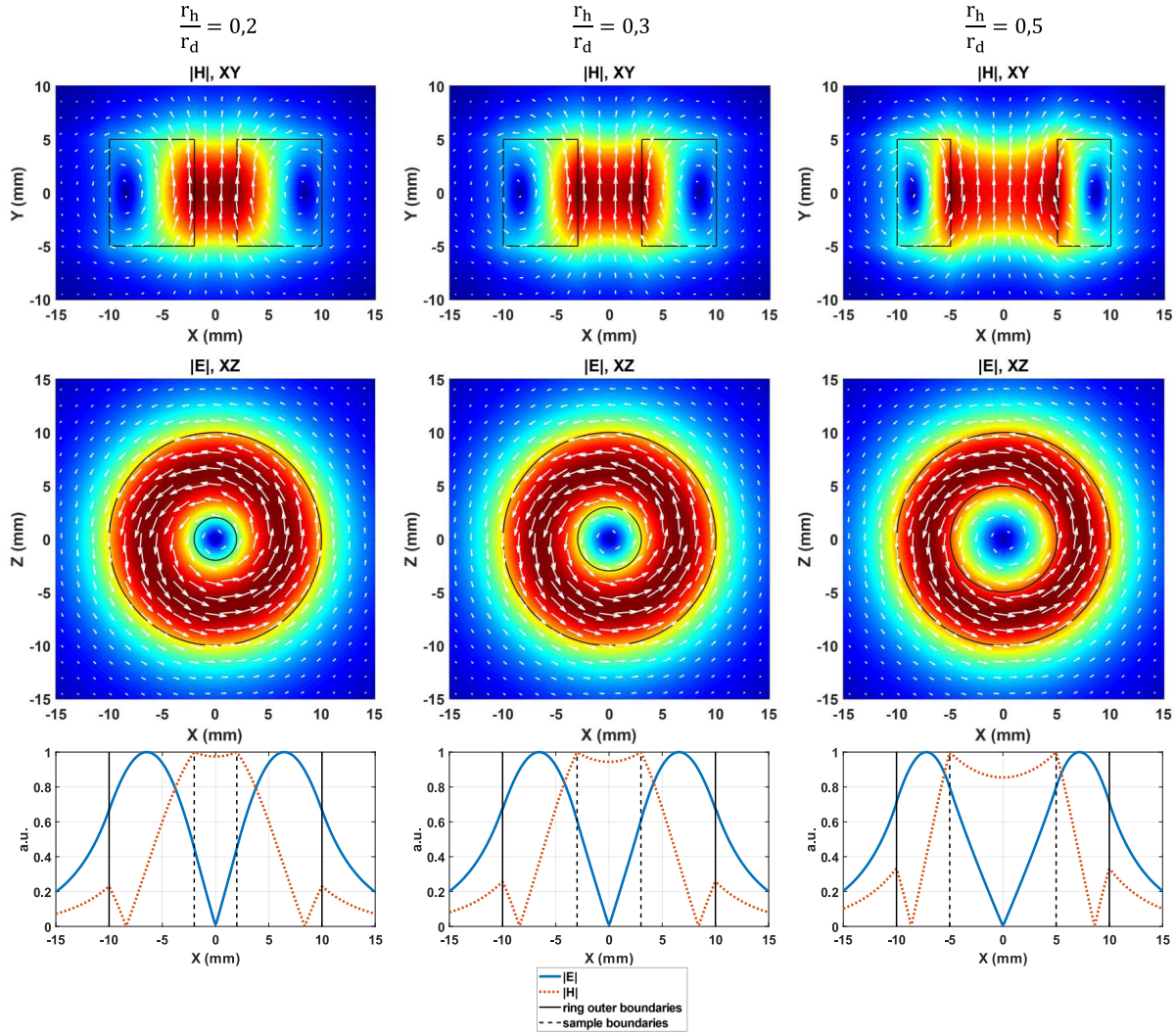

Fig. 7. Normalized field maps of a dielectric ring (permittivity 500, height 10 mm, and outer diameter 20 mm) filled with a sample of permittivity 50 for different inner to outer radii ratios. Top line: modulus of the total magnetic field. Middle line: modulus of the total electric field. Bottom line: field lines of the total electric (blue solid line) and magnetic (orange dotted line) fields in the center of the resonator ($y = 0$). The maps and field lines are normalized to the maximum value of the field modulus. Linear color scale from 0 to 1.

Next, combining the last two equations of (12) and (8) leads to the set of equations (14), which is equivalent to the eigenvalue problem of a planar dielectric waveguide [25]. In the same manner, (14) is numerically solved with respect to β. It gives several solutions depicting the different planar waveguide modes, as shown by the dashed dispersion curves in Fig. 6

$$\beta \tan\left(\beta \frac{L}{2}\right) = \gamma \coth\left(\gamma \frac{h-L}{2}\right)$$
$$\gamma = \sqrt{(\epsilon_r - 1)k_0^2 - \beta^2}. \tag{14}$$

The modes of the dielectric resonators are deduced from the intersection of the abovementioned two sets of solutions. The lowest β intersection point corresponds to the first-order mode of the planar waveguide combined with the first-order mode of the circular waveguide, that is, the $TE_{01\delta}$ mode of the dielectric resonator, as shown in Fig. 6. The other wavenumber components are deduced from the β value using (8).

Fig. 7 shows some examples of the field maps estimated with this approach for a dielectric ring of outer radius $r_d = 10$ mm, height $L = 10$ mm, and relative permittivity $\epsilon_r = 500$, filled with a sample of varying radius r_h and relative permittivity $\epsilon_{r,samp} = 50$. The smaller the ratio r_h/r_d, the more the magnetic field confined within the sample with high intensity, while the region in which the electric field is minimum is only slightly affected in terms of lateral dimensions when the sample diameter increases, as shown in Fig. 7 (bottom line).

The validity of this approach to estimate the field distribution is compared with numerical simulations from the CST Studio Eigenmode Solver. In particular, it is quantified through the field-normalized root-mean-squared error (FD-NRMSE) expressed in (15): at each point r_n of the selected grid Ω, the relative error between the reference field component U_{ref} and the SAM field component U is computed, and the FD-NRMSE is the squared sum of all these error terms divided by the number of points of the grid N_{pts}^{Ω}

$$\text{FD-NRMSE} = \frac{1}{N_{pts}^{\Omega}} \sum_{n=1}^{N_{pts}^{\Omega}} \left(\frac{U(\mathbf{r_n}) - U_{ref}(\mathbf{r_n})}{U_{ref}(\mathbf{r_n})} \right)^2. \tag{15}$$

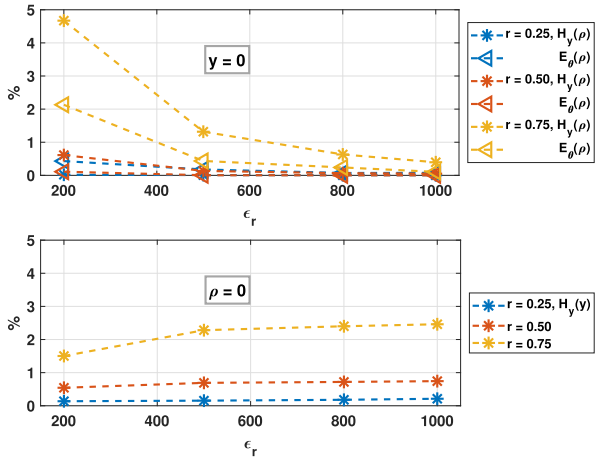

Fig. 8. Error on the field distribution within the sample depending on the relative permittivity ϵ_r of the probe dielectric material, for three values of ratio $r = r_h/r_d$.

Fig. 8 shows the quantitative values of this error. The reference field is exported from numerical simulations (CST Studio, Eigenmode Solver). The figure shows the FD-NRMSE computed in the sample along the lines of equation $y = 0$ (top graph) and $\rho = 0$ (bottom graph). It is plotted as a function of the relative permittivity of the dielectric material of the probe. In each case, the $TE_{01\delta}$ mode of the corresponding disk resonator is adjusted to the Larmor frequency at 17.2 T (730 MHz) via its diameter, as covered in Section II-A. The resonator height is kept equal to 10 mm. The FD-NRMSE never exceeds 5%. Increasing the permittivity, which involves a higher confinement of the mode in the probe, also leads to an improvement in the accuracy of the semi-analytical method regarding the radial field distribution.

III. Power Losses Estimation

When designing a dielectric probe for MRI, one key feature that must be quantified is the proportion of the input power lost during acquisition, be it in the probe itself or in the sample. This is a necessary step to estimate the noise induced by these losses. In this section, we propose a simplified approach to estimate the contributions to power losses from the probe and from the sample. This will be used in Section IV to evaluate the SNR provided by a dielectric probe as a function of its geometrical and EM properties.

When an object of volume Ω and material of complex permittivity $\epsilon = \epsilon' - j\epsilon''$ (with our notations $\epsilon' = \epsilon_0\epsilon_r \geq 0$ and $\epsilon'' = \epsilon' \tan\delta$) is immersed in an EM field, energy is dissipated in the form of heat [35].

This is caused by two phenomena: electric conduction if the density of free electrons is nonzero and bound charges polarization [24]. In our notation, the material loss tangent includes both contributions: $\tan\delta = \tan\delta_{|\text{cond}} + \tan\delta_{|\text{polar}}$. Power losses in the object are expressed as the integral over its volume Ω of the power loss density p, as in the following [35]:

$$P_{\text{loss}} = \int_{\Omega} p(\mathbf{r}) \mathrm{d}^3\mathbf{r}$$
$$p = \frac{1}{2}\omega\epsilon''|\overrightarrow{\mathrm{E}}|^2. \tag{16}$$

High-permittivity materials that can be used to build dielectric probe are ceramics, as in [4], [5], and [23]. Such materials are described by their experimentally measured real permittivity and total loss tangent [36]. Biological samples on the other hand are electrically conductive with a significant contribution as they contain water. In that case, the power loss density reduces to

$$p_{\text{samp}} = \frac{1}{2}\sigma|\overrightarrow{\mathrm{E}}|^2. \tag{17}$$

Noise (loss) involved in the signal acquisition during MRM experiment comes from the resistance of the dielectric ring resonator and from the conductive sample placed within the ring. As evoked in Section II, the $TE_{01\delta}$ eigenmode of the ring resonator is very similar to that of the corresponding disk resonator (no hole). Therefore, in order to provide analytical expressions for the dielectric losses in each subvolume, the following approximations are used.

1) Losses in the dielectric resonator are small enough not to influence the field distribution. Therefore, the EM-field expression used for computing dielectric losses is that of a lossless resonator.
2) The electric field distribution of the ring resonator is assumed equal to that of the disk resonator ($\overrightarrow{\mathrm{E}}^{\text{disk}}(\mathbf{r})$) and the field leakages through lateral boundaries can be neglected. As a result, the radial wavenumber α is quantified as x_{01}/r_d, where x_{01} is the first zero of the zeroth-order Bessel function of the first kind: $J_0(x_{01}) = 0$.
3) The magnetic field decrease within the sample is due to its relative permittivity being different from that of the ring and quantified by the so-called penalty coefficient $\tau = H_0^{\text{sample}}/H_0^{\text{disk}}$ with $H_0 = |\overrightarrow{\mathrm{H}}(\rho = 0, y = 0)|$. The field decrease and the way the coefficient is estimated are shown in Fig. 9. Its maximum value is 1, which corresponds to the disk ($\Delta\epsilon_r = 0$), and it decreases to zero with the increasing permittivity contrast. In practice, τ is estimated from the semi-analytically computed distributions considering field leakages at the boundaries, by comparing the H_0 value in the disk and in the sample excited by the ring resonator, with a correcting factor applied to ensure the following condition: $|\overrightarrow{\mathrm{H}}^{\text{ring}}(\rho = r_h, y = 0)| = |\overrightarrow{\mathrm{H}}^{\text{disk}}(\rho = r_h, y = 0)|$.

The two contributions for the losses are, therefore, expressed as the following.

Ring Resonator Losses

$$P_{\text{loss}}^{\text{ring}} = \frac{1}{2}\epsilon_0\epsilon_r\omega\tan\delta\int_{V_{\text{ring}}}|\overrightarrow{\mathrm{E}}^{\text{disk}}(\mathbf{r})|^2\mathrm{d}^3\mathbf{r} \tag{18}$$

$$P_{\text{loss}}^{\text{ring}} = \Delta\epsilon_0\epsilon_r\omega\tan\delta L_{\text{eff}}\left(H_0^{\text{disk}}\right)^2\int_{r_h}^{r_d}\rho J_1^2(\alpha\rho)\mathrm{d}\rho \tag{19}$$

$$\Delta = 2\pi\left(\frac{\omega\mu_0}{2\alpha}\right)^2 \tag{20}$$

$$L_{\text{eff}} = \left(1 + \frac{\sin(\beta L)}{\beta L}\right)L \tag{21}$$

$$P_{\text{loss, norm}}^{\text{ring}} = \Delta\epsilon_0\epsilon_r\omega\tan\delta L_{\text{eff}}\int_{r_h}^{r_d}\rho J_1^2(\alpha\rho)\mathrm{d}\rho. \tag{22}$$

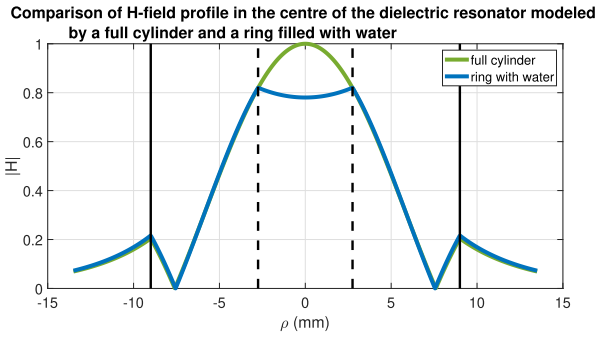

Fig. 9. H-field (absolute value of the total field) decrease in water (semi-analytical method). Full (respectively, dashed) lines indicate the outer (respectively, inner) boundaries of the ceramic probe. The penalty factor τ defined in III is here estimated by the value of the blue curve in $\rho = 0$.

Sample Losses

$$\mathrm{P}_{\mathrm{loss}}^{\mathrm{sample}} = \frac{1}{2}\sigma_{\mathrm{sample}}\tau^2 \int_{V_{\mathrm{samp}}} |\overrightarrow{\mathrm{E}}^{\mathrm{disk}}(\mathbf{r})|^2 \mathrm{d}^3\mathbf{r}$$

$$= \Delta\sigma_{\mathrm{sample}}\mathrm{L}_{\mathrm{eff}}\left(\tau \mathrm{H}_0^{\mathrm{disk}}\right)^2 \int_0^{r_{\mathrm{h}}} \rho \mathrm{J}_1^2(\alpha\rho)\mathrm{d}\rho \quad (23)$$

$$\mathrm{P}_{\mathrm{loss,\ norm}}^{\mathrm{sample}} = \Delta\sigma_{\mathrm{sample}}\mathrm{L}_{\mathrm{eff}} \int_0^{r_h} \rho \mathrm{J}_1^2(\alpha\rho)\mathrm{d}\rho. \quad (24)$$

To develop fully these expressions for dielectric losses, the integrals of the square of the first kind, first-order Bessel function J_1 are derived from (25) from [37] generalized to arbitrary boundaries in (26)

$$\forall u \in R,$$

$$\int_0^u \rho \mathrm{J}_1^2(\alpha\rho)\mathrm{d}\rho = \frac{u^2}{2}\left[\mathrm{J}_1^2(\alpha u) - \mathrm{J}_0(\alpha u)\mathrm{J}_2(\alpha u)\right] \quad (25)$$

$$\forall (u, v) \in R^2,$$

$$\int_v^u \rho \mathrm{J}_1^2(\alpha\rho)\mathrm{d}\rho = \frac{u^2}{2}\left[\mathrm{J}_1^2(\alpha u) - \mathrm{J}_0(\alpha u)\mathrm{J}_2(\alpha u)\right] - \frac{v^2}{2}\left[\mathrm{J}_1^2(\alpha v) - \mathrm{J}_0(\alpha v)\mathrm{J}_2(\alpha v)\right]. \quad (26)$$

The model developed for the dielectric loss estimation was compared with the numerical simulations performed with the CST Microwave Studio Eigenmode Solver, which ignores the material losses. In particular, a comparison was performed on the penalty factor τ and the normalized power loss term $\tau^2\mathrm{P}_{\mathrm{loss,\ norm}}^{\mathrm{sample}} + \mathrm{P}_{\mathrm{loss,\ norm}}^{\mathrm{ring}}$ in the case of a dielectric ring of permittivity 500, height 10 mm, and outer diameter 20 mm; the ceramic loss tangent was 10^{-3}.

Regarding the validation of the penalty factor estimation, the sample permittivity varied between 1 and 100 and the inner over outer diameter ratio $\mathrm{r} = r_{\mathrm{h}}/r_{\mathrm{d}}$ was 0.2, 0.3, and 0.5, while the normalized power losses were studied for ratio equal to 0.3 for varying sample properties (permittivity and conductivity).

The penalty factor τ quantifies the decrease in H-field in the center of the sample due to the permittivity contrast between the ceramic material and the sample medium. As shown in Fig. 10, the lower the sample permittivity, the lower the penalty factor and the H-field magnitude. The magnetic field also decreases when increasing the sample diameter, that is, the r ratio, and so does the error on the penalty factor estimation, which is otherwise barely affected by the sample

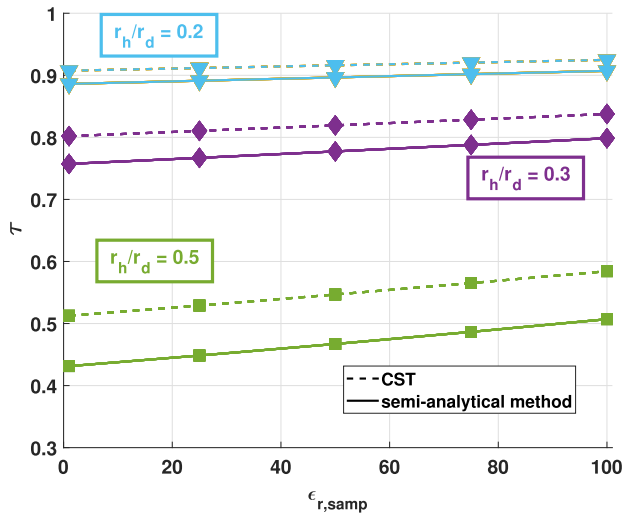

Fig. 10. Comparison of the value of the penalty factor estimated with the developed field distribution model, to the value from numerical simulations, as a function of the sample permittivity.

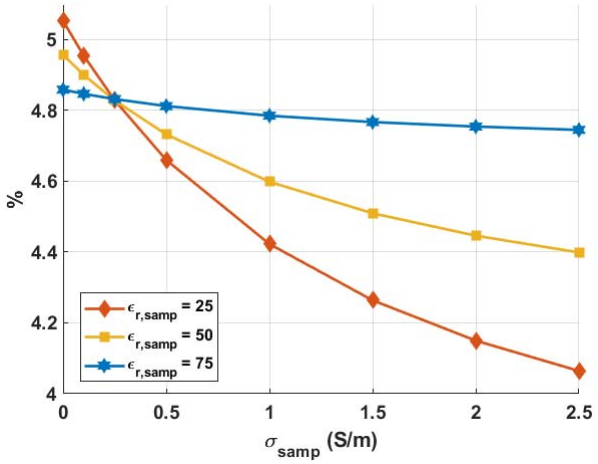

Fig. 11. Comparison of semi-analytical method and numerical simulation results in terms of normalized power losses term $\tau^2\mathrm{P}_{\mathrm{loss,\ norm}}^{\mathrm{sample}} + \mathrm{P}_{\mathrm{loss,\ norm}}^{\mathrm{ring}}$, as a function of the sample conductivity.

permittivity value. For the three r ratio values considered here 0.2, 0.3, and 0.5, the maximum relative errors between the semi-analytical method and the full-wave simulations is 2.4%, 5.6%, and 15.8%, respectively. In the last case, the model fails to describe properly the H-field distribution. The reason for this is that, as shown in Fig. 7, the E-field can no longer be assumed to be zero in the sample as its diameter increases. In consequence, we consider that the model should not be used for a diameter ratio higher than 0.5.

Fig. 11 shows the relative error between the normalized total power losses from the developed model for the field distribution and the Eigenmode Solver. The error is less than 5.1% in all the configurations considered here, which already cover a wide range of biological samples.

IV. SNR Estimation

The SNR factor, defined in (27), can be expressed in terms of $\mathrm{H}_0^{\mathrm{probe}}$ the magnetic field in the sample and $\mathrm{P}_{\mathrm{loss}}^{\mathrm{probe}}$ the total dielectric losses (from the probe and the sample). This quantity

u_{SNR} [see (27)] is useful not only in designing a ceramic probe with optimal parameters but also in comparing this probe performance with other MRM coil types, for example, the commonly used solenoid. It is equivalent, ignoring a multiplication factor of $\sqrt{2}$, to the resonator efficiency used by Mett *et al.* [21], [22] in their lumped-element equivalent circuit approach

$$u_{\mathrm{SNR}}^{\mathrm{probe}} = \frac{\mathrm{H}_0^{\mathrm{probe}}}{\sqrt{\mathrm{P}_{\mathrm{loss}}^{\mathrm{probe}}}}. \tag{27}$$

Considering the model hypothesis presented in III, the magnetic field within the sample is expressed as the product of the penalty factor τ with the H-field amplitude in the disk H_0^{disk}. The power losses, accounting for electric field–sample interactions, are expressed by (19) and (23). The H-field amplitude in the disk simplifies between the numerator and the denominator, and (27) becomes

$$\begin{aligned} u_{\mathrm{SNR}}^{\mathrm{DR}} &= \frac{\tau \mathrm{H}_0^{\mathrm{disk}}}{\sqrt{\mathrm{P}_{\mathrm{loss}}^{\mathrm{sample}} + \mathrm{P}_{\mathrm{loss}}^{\mathrm{ring}}}} \\ &= \frac{\tau}{\sqrt{\tau^2 \mathrm{P}_{\mathrm{loss,\ norm}}^{\mathrm{sample}} + \mathrm{P}_{\mathrm{loss,\ norm}}^{\mathrm{ring}}}}. \end{aligned} \tag{28}$$

The model proposed for the SNR factor estimation, herein after named semi-analytical model (SAM), was applied to the case of a ceramic resonator prototype (outer diameter $2r_{\mathrm{d}} = 18$ mm, inner diameter $2r_{\mathrm{h}} = 5.6$ mm, height $\mathrm{L} = 10$ mm, relative permittivity $\epsilon_{\mathrm{r}} = 536$, and loss tangent $\tan\delta = 8.10^{-4}$) and was experimentally validated in [23]. In this paragraph, we compare the SNR factor provided by this probe, as a function of the sample conductivity, for two distinct values of sample relative permittivities, 50 and 81. Numerical simulations were performed using the CST Microwave Studio Frequency Domain Solver, with the dielectric ring resonator and a sample of diameter 4.5 mm and height 20 mm. In this configuration, the probe was fed through inductive coupling with a 3 mm loop placed at 3.8 mm from it, and is placed in the center of a metallic cylindrical shell representing the MR device bore (material: perfect electric conductor; total length along z-axis: 600 mm; diameter: 91 mm). This is the most realistic case, compared with the simulations using the Eigenmode Solver, in which no source is exciting the resonant mode. The SAM was also compared with a "combined method," in which the SNR factor is computed by estimating each variable in (27) with the discretized E-field (mesh step 0.2 mm) exported from the simulation software (Eigenmode Solver). In particular, dielectric losses are derived by integrating the squared E-field multiplied by the local loss term [see (16)] with the rectangle rule. Fig. 12 shows these results and Table I gives an example of numerical values for the computed parameters of (27).

For both permittivities, the CST, combined method, and SAM curves all follow the same decreasing trend when the sample conductivity is increased. The maximum relative error value between the semi-analytical and combined methods, and the realistic numerical simulations was estimated at 8% and 5%, respectively. Both approaches produce results that are on the same order as errors intrinsic to the experimental

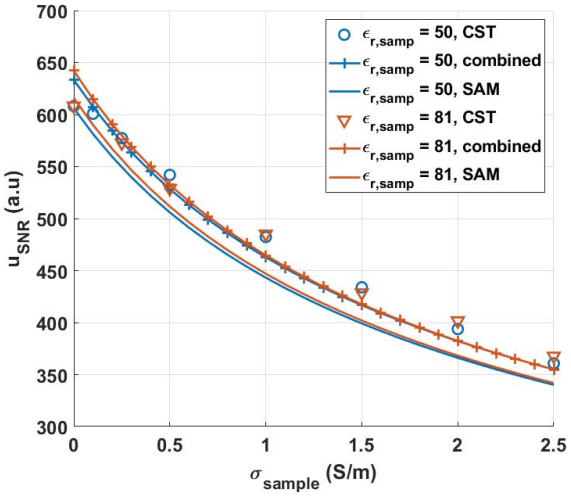

Fig. 12. Comparison, in terms of SNR factor, of (*SAM*) with numerical simulations results (frequency domain solver of *CST* Microwave Studio) and (28) applied to the E-field distribution from the software Eigenmode Solver (*combined*).

TABLE I
COMPUTED VARIABLES FOR A SAMPLE OF PERMITTIVITY 50 AND CONDUCTIVITY 1 s/m

	SAM	Eigenmode solver
τ	0,77	0,81
$P_{loss,norm}$	$0{,}30.10^{-5}$	$0{,}31.10^{-5}$
u_{SNR}	445	463

measurements of SNR in MRM, and these results also validate the approximations from Section III.

In the framework of the development of an MRM probe, comparison of the SNR reachable by the dielectric probe with the conventional probe designs is of great interest in order to maximize the achievable SNR. In the case of the proposed sample and MR system described in Section I, the reference volume probe is the solenoid probe, and the SNR factor can be expressed following the guidelines described in [38] and [12]. An example of such a comparative study can be found in [23].

V. DISCUSSION

The theoretical tools presented in this article aim at assisting the design of dielectric probes for MRI. In this framework, the proposed approach is a simplified modeling of such a resonator that enables to estimate its first TE-mode frequency and the expected SNR factor, without relying on numerical simulations on initial examination. As presented in Sections II to IV, the accuracy of this method is satisfying for designing an optimized first prototype of such a probe. It was tested for realistic values of ceramic material permittivities [36] and usual values of biological samples permittivities (1–100) in the MRI frequency range (from 100 MHz to 1 GHz). However, another aspect that was not undertaken previously is its computation time. Table II illustrates this point for the probe developed for [23] and for two different samples. The provided delays are averaged over ten trials for each computed variables (frequency and SNR factor) and for each method. The margin of error is not provided if it is strictly

TABLE II
COMPARISON OF COMPUTATION TIMES IN THE CASE OF THE DIELECTRIC PROBE PRESENTED IN [23]

		Frequency		u_{SNR}	
$\epsilon_{\mathrm{r,samp}}$	σ_{samp}	SAM	Eigenmode solver	SAM	Frequency domain solver
50	1 S/m	4 ms	4 min 31 s $\pm$ 2 s	7 s	1 min 29 $\pm$ 2 s
81	1,5 S/m	4 ms	4 min 28 s $\pm$ 5 s	7 s	1 min 32 s $\pm$ 1 s

subsecond. The computation is performed on a computer with 64 GB of RAM and an Intel Xeon processor (CPU E5-1630 v4). Regarding the SNR factor estimation with the Frequency Domain Solver of CST Studio (frequency range 700–780 MHz, tetrahedral mesh), the effective estimation delay is the given value, corresponding to the solver time, plus the time to tune and match the feeding loop at the desired Larmor frequency. From these results, there is no doubt that the theoretical approach is much faster than the numerical simulations.

VI. CONCLUSION

In summary, this article addresses the topic of ceramic probes developed for MRM. In particular, it proposes a semi-analytical method, based on the study of the first transverse electric mode of a high-permittivity dielectric ring, to estimate its resonance frequency and a measure of the SNR for evaluating the imaging performance of such probe. The knowledge of this quantity enables comparison with the standard probe configurations and can be used as design guideline to optimize the dielectric ring EM and geometrical properties.

REFERENCES

[1] L. Ciobanu, *Microscopic Magnetic Resonance Imaging: A Practical Perspective*. Singapore: Pan Stanford, 2017, chs. 2–7.

[2] H. Chen and R. Tycko, "Low-temperature magnetic resonance imaging with 2.8 μm isotropic resolution," *J. Magn. Reson.*, vol. 287, pp. 47–55, Feb. 2018. [Online]. Available: http://www.sciencedirect.com/science/article/pii/S1090780717303087

[3] A. G. Webb, "Dielectric materials in magnetic resonance," *Concepts Magn. Reson. A*, vol. 38A, no. 4, pp. 148–184, Jul. 2011.

[4] K. Haines, T. Neuberger, M. Lanagan, E. Semouchkina, and A. G. Webb, "High Q calcium titanate cylindrical dielectric resonators for magnetic resonance microimaging," *J. Magn. Reson.*, vol. 200, no. 2, pp. 349–353, Oct. 2009.

[5] T. Neuberger *et al.*, "Design of a ceramic dielectric resonator for NMR microimaging at 14.1 tesla," *Concepts Magn. Reson. B, Magn. Reson. Eng.*, vol. 33B, no. 2, pp. 109–114, Apr. 2008.

[6] D. Kajfez and P. Guillon, *Dielectric Resonators*. Atlanta, GA, USA: Noble Publishing Corporation, 1998, chs. 3.5, 1, 4, and 4.4, pp. 90, 3, 185, 113, and 128.

[7] K. W. Leung, E. H. Lim, and X. S. Fang, "Dielectric resonator antennas: From the basic to the aesthetic," *Proc. IEEE*, vol. 100, no. 7, pp. 2181–2193, Jul. 2012.

[8] S. Long, M. McAllister, and L. Shen, "The resonant cylindrical dielectric cavity antenna," *IEEE Trans. Antennas Propag.*, vol. 31, no. 3, pp. 406–412, May 1983.

[9] S. J. Fiedziuszko, "Dual-mode dielectric resonator loaded cavity filters," *IEEE Trans. Microw. Theory Techn.*, vol. MTT-30, no. 9, pp. 1311–1316, Sep. 1982.

[10] X.-P. Liang and K. A. Zaki, "Modeling of cylindrical dielectric resonators in rectangular waveguides and cavities," *IEEE Trans. Microw. Theory Techn.*, vol. 41, no. 12, pp. 2174–2181, Dec. 1993.

[11] S.-W. Chen and K. A. Zaki, "Dielectric ring resonators loaded in waveguide and on substrate," *IEEE Trans. Microw. Theory Techn.*, vol. 39, no. 12, pp. 2069–2076, Dec. 1991.

[12] K. R. Minard and R. A. Wind, "Solenoidal microcoil design—Part II: Optimizing winding parameters for maximum signal-to-noise performance," *Concepts Magn. Reson.*, vol. 13, no. 3, pp. 190–210, 2001.

[13] D. I. Hoult and R. E. Richards, "The signal-to-noise ratio of the nuclear magnetic resonance experiment," *J. Magn. Reson.*, vol. 24, no. 1, pp. 71–85, 1976.

[14] D. Kajfez, A. W. Glisson, and J. James, "Computed modal field distributions for isolated dielectric resonators," *IEEE Trans. Microw. Theory Techn.*, vol. MTT-32, no. 12, pp. 1609–1616, Dec. 1984.

[15] J. Van Bladel, "On the resonances of a dielectric resonator of very high permittivity," *IEEE Trans. Microw. Theory Techn.*, vol. MTT-23, no. 2, pp. 199–208, Feb. 1975.

[16] R. De Smedt, "Correction due to a finite permittivity for a ring resonator in free space," *IEEE Trans. Microw. Theory Techn.*, vol. MTT-32, no. 10, pp. 1288–1293, Oct. 1984.

[17] M. Verplanken and J. Van Bladel, "The magnetic-dipole resonances of ring resonators of very high permittivity," *IEEE Trans. Microw. Theory Techn.*, vol. MTT-27, no. 4, pp. 328–333, Apr. 1979.

[18] H. Y. Yee, "Natural resonant frequencies of microwave dielectric resonators (correspondence)," *IEEE Trans. Microw. Theory Techn.*, vol. MTT-13, no. 2, p. 256, Mar. 1965.

[19] S. B. Cohn, "Microwave bandpass filters containing high-Q dielectric resonators," *IEEE Trans. Microw. Theory Techn.*, vol. MTT-16, no. 4, pp. 218–227, Apr. 1968.

[20] T. Itoh and R. S. Rudokas, "New method for computing the resonant frequencies of dielectric resonators (short papers)," *IEEE Trans. Microw. Theory Techn.*, vol. MTT-25, no. 1, pp. 52–54, Jan. 1977.

[21] R. R. Mett, J. W. Sidabras, I. S. Golovina, and J. S. Hyde, "Dielectric microwave resonators in TE_{011} cavities for electron paramagnetic resonance spectroscopy," *Rev. Sci. Instrum.*, vol. 79, no. 9, 2008, Art. no. 094702.

[22] R. R. Mett, J. W. Sidabras, J. R. Anderson, C. S. Klug, and J. S. Hyde, "Rutile dielectric loop-gap resonator for X-band EPR spectroscopy of small aqueous samples," *J. Magn. Reson.*, vol. 307, Oct. 2019, Art. no. 106585.

[23] M. A. C. Moussu *et al.*, "Systematic analysis of the improvements in magnetic resonance microscopy with ferroelectric composite ceramics," *Adv. Mater.*, vol. 31, no. 30, 2019, Art. no. 1900912.

[24] S. J. Orfanidis, *Electromagnetic Waves and Antennas*, 2003, chs. 7.4, 1.14, pp. 23–25 and 289. [Online]. Available: http://eceweb1.rutgers.edu/~orfanidi/ewa

[25] K. Zhang, D. Li, K. Chang, K. Zhang, and D. Li, *Electromagnetic Theory for Microwaves and Optoelectronics*, 2nd ed. Springer, 2008, chs. 6.2, 6.8 and C.4, pp. 327–333, 387–394 and 685.

[26] R. K. Mongia and P. Bhartia, "Dielectric resonator antennas—A review and general design relations for resonant frequency and bandwidth," *Int. J. Microw. Millim.-Wave Comput.-Aided Eng.*, vol. 4, no. 3, pp. 230–247, Jul. 1994.

[27] D. M. Pozar, *Microwave Engineering*, 4th ed. Hoboken, NJ, USA: Wiley, 2012.

[28] A. A. Kishk, A. W. Glisson, and G. P. Junker, "Bandwidth enhancement for split cylindrical dielectric resonator antennas," *Prog. Electromagn. Res.*, vol. 33, pp. 97–118, 2001.

[29] M. Rotaru and J. K. Sykulski, "Numerical investigation on compact multimode dielectric resonator antennas of very high permittivity," *IET Sci., Meas. Technol.*, vol. 3, no. 3, pp. 217–228, May 2009.

[30] Y. Garault and P. Guillon, "Higher accuracy for the resonance frequencies of dielectric resonators," *Electron. Lett.*, vol. 12, no. 18, pp. 475–476, 1976.

[31] R. F. Harrington, *Time-Harmonic Electromagnetic Fields*. New York, NY, USA: McGraw-Hill, 1961, chs. 7–4, pp. 321–325.

[32] J. Sheen, "A dielectric resonator method of measuring dielectric properties of low loss materials in the microwave region," *Meas. Sci. Technol.*, vol. 19, no. 5, May 2008, Art. no. 055701.

[33] E. Snitzer, "Cylindrical dielectric waveguide modes," *J. Opt. Soc. Amer.*, vol. 51, no. 5, pp. 491–498, May 1961.

[34] Y. V. Shestopalov and E. A. Kuzmina, "On a rigorous proof of the existence of complex waves in a dielectric waveguide of circular cross section," *Prog. Electromagn. Res. B*, vol. 82, pp. 137–164, 2018.

[35] R. Petit, *Ondes électromagnétiques en radioélectricité et en optique*, vol. 2, 2nd ed. Paris, France: Masson, 1993, ch. IV.5, pp. 97–99.
[36] E. A. Nenasheva *et al.*, "Low loss microwave ferroelectric ceramics for high power tunable devices," *J. Eur. Ceram. Soc.*, vol. 30, no. 2, pp. 395–400, Jan. 2010.
[37] F. Bowman, *Introduction to Bessel Functions*. Chelmsford, MA, USA: Courier Corporation, 2012, ch. 6, p. 101.
[38] K. R. Minard and R. A. Wind, "Solenoidal microcoil design. Part I: Optimizing RF homogeneity and coil dimensions," *Concepts Magn. Reson.*, vol. 13, no. 2, pp. 128–142, 2001.

Marine A. C. Moussu received the Engineering degree (M.Sc. equivalent) from the École Supérieure de Physique et de Chimie Industrielles de la Ville de Paris (ESPCI Paris), Paris, France, in 2017, and the M.Sc. degree in acoustics and the international Europhotonics M.Sc. degree in photonics from Aix-Marseille Université Marseille, France, in 2017. She is currently pursuing the Ph.D. degree with Multiwave Imaging, Marseille, and the Institut Fresnel, Aix-Marseille Université, Marseille, France.

Her research interests include wave physics applied to imaging and focusing, electromagnetic (EM) modeling, and inverse problems.

Redha Abdeddaim was born in Alger, Algeria, in 1979. He received the Ph.D. degree in physics from Paris X University, Paris, France, in 2007.

He is currently an Assistant Professor with Aix-Marseille Université, Marseille, France. His current research interests include metamaterials, antennas, and magnetic resonance imaging (MRI) coils.

Marc Dubois received the Ph.D. degree in condensed matter from Université Paris Diderot, Paris, France, in 2014.

He is currently a Post-Doctoral Researcher with the Center for Magnetic Resonance in Biology and Medicine, Marseille, France, and the Institut Fresnel, Marseille. His current research interests include metamaterials and electromagnetism for magnetic resonance imaging (MRI) applications.

Elodie Georget received the Engineering degree (M.Sc. equivalent) from the National Institute of Applied Sciences (INSA), Rennes, France, in 2011, specializing in communication systems and networks, and the Ph.D. degree in physics from the Centre National de la Recherche Scientifique (CNRS) Research Laboratory, Institut Fresnel, Aix Marseille University, Marseille, France, in 2014.

She is experienced in the field of electromagnetism, working on the development of experimental techniques like radio-frequency (RF) antennas for magnetic resonance imaging (MRI), metrology, and the electromagnetic (EM) characterization of materials. She worked with Commissariat à l'Energie Atomique et aux Energies Alternatives (CEA)-Neurospin, Gif-sur-Yvette, France, for two years to push the boundaries on ultrahigh field MRI coils. She is currently the Head of the subsidiary Multiwave Imaging, Marseille, and also the Head of MRI Technologies.

Andrew G. Webb (Member, IEEE) received the bachelor's degree in chemistry from the University of Bristol, Bristol, U.K., and the Ph.D. degree from the University of Cambridge, Cambridge, U.K., in 1986 and 1989, respectively.

After a post-doctoral position with the Department of Radiology, University of Florida, Gainesville, FL, USA, he joined the Faculty of the Department of Electrical and Computer Engineering, University of Illinois at Urbana–Champaign, Champaign, IL, USA. He was appointed as a Full Professor in 2000 and worked for three years in the Department of Physics, University of Wurzburg, Würzburg, Germany, on the Humboldt Fellowship. In 2008, he was appointed to run the newly formed C.J. Gorter Center, Department of Radiology, Leiden University Medical Center, Leiden, The Netherlands. Recently, his laboratory has moved into the areas of sustainable open-source low-field MRI for developing countries funded by the Simon Stevin Preis. In addition to over 300 peer-reviewed publications, he has authored four academic text books on medical imaging and biomedical instrumentation. His main research areas are radio-frequency (RF) design for high-field magnetic resonance imaging (MRI) and translation of new engineering concepts into the clinic supported by an European Research Council (ERC) Advanced Grant.

Dr. Webb is currently an Associate Editor of *Magnetic Resonance in Medicine* and serves on the editorial board of several other MR journals. In 2020, he will be the President of the European Society of Magnetic Resonance in Medicine and Biology. Most meaningfully, in 2010, he founded the Nadine Barrie Smith Trust, which supports four student fellowships per year for women in science and engineering.

Elizaveta Nenasheva received the M.S. degree in physics from ElectroTechnical University, Saint Petersburg, Russia, in 1974, and the Ph.D. degree in physics from the Giricond Research Institute, Saint Petersburg, in 1981.

In 2006, 2007, and 2010, she was a Visiting Professor of the High Energy Physics Department (HEP) Division of Argonne National Laboratory (ANL), Argonne, IL, USA, and took part in researches of more than ten grants of the Department of Energy of USA. She is an Internationally Recognized Expert in designing of low-loss microwave ceramic and ferroelectrics. She has also been active in the area of smart materials development and ceramic technology applications for advanced accelerators research and development. She was the Chief of the Department of Microwave Ceramics, Giricond Research Institute, Saint Petersburg, where she is currently the Director of Ceramics Company. She has published more than 140 articles and holds 50 national and world patents in the field of microwave ceramic compositions and ferroelectric technology development.

Pavel Belov was born in the Union of Soviet Socialist Republics (USSR) in 1977. He received the M.Sc. degree (Hons.) in applied mathematics from ITMO University, St. Petersburg, Russia, in 2000. He defended two Ph.D. theses: one in optics at ITMO University in 2003; and the second one in radioengineering at the Helsinki University of Technology, Espoo, Finland, in 2006.

He is currently the Dean of the Physics and Engineering Faculty and the Head of the Research Center of Nanophotonics and Metamaterials, ITMO University. His current research interests include metamaterials, plasmonics, electromagnetics, nanophotonics, antennas, and nanostructures.

Stanislav Glybovski (Member, IEEE) was born in Syktyvkar, Russia, in 1987. He received the M.Sc. and Ph.D. degrees in radiophysics from St. Petersburg Polytechnic State University, Saint Petersburg, Russia, in 2010 and 2013, respectively.

He is currently a Senior Researcher with the Department of Physics and Engineering, ITMO University, Saint Petersburg. His current research interests include antennas and microwave devices, computational electromagnetics, metamaterials, and magnetic resonance imaging (MRI).

Luisa Ciobanu received the Ph.D. degree in physics from The Ohio State University, Columbus, OH, USA, in 2002.

She then went on to do Post-Doctoral training with the Department of Electrical and Computer Engineering, University of Illinois at Urbana–Champaign, Champaign, IL, USA. After her post-doc, she has held research appointments with the Beckman Institute, University of Illinois at Urbana–Champaign and Pfizer, Inc., Ann Arbor, MI, USA. In 2007, she joined NeuroSpin, Commissariat à l'Energie Atomique et aux Energies Alternatives (CEA)-Saclay, Gif-sur-Yvette, France, where she heads the NeuroPhysics Team. Her primary research interests include MR microscopy and its application to neuroscience investigations and the development of novel functional magnetic resonance imaging (MRI) techniques for ultrahigh magnetic field imaging.

Stefan Enoch received the Ph.D. degree from Aix-Marseille University, Marseille, France, in 1997.

He became an Assistant Professor with Aix-Marseille University in 1998, and joined Centre National de la Recherche Scientifique (CNRS), Paris, France, in 2001. He has been the Director of the Institut Fresnel, Marseille, for height years. He is currently a Senior Researcher with the CNRS and the Deputy Vice President for Sciences and Technologies of Aix-Marseille Université. His research combines fundamental and applied research. His research involves the theory, modeling, and engineering of the interaction between the waves and their environment. Though his main contributions are in optics and more recently in microwaves, he has also made significant contributions to mechanical waves in solids. His work in optics started with fundamental investigations of the properties of photonic crystals and has since shifted to the properties of metamaterials and their applications. He is considered an internationally recognized researcher on theory and modeling for nanophotonics. He has published about 150 research articles in top ranked journals, and he has given more than 40 invited and plenary presentations at a variety of conferences. His publications have been cited over 10 300 times and his H-index is 46 (source Google Scholar). He recently led the Future and Emerging Technologies (FET)-OPEN M-CUBE Project that aims to improve the resolution of magnetic resonance imaging (MRI) by generating ultrahigh fields using metamaterial antennas. The grant has ten partners, including two Small to Medium Enterprises, and has a budget of €3.9M. Briefly, the quality of images of ultrahigh field MRI scanners is limited by spatial inhomogeneities of the radio-frequency field. He has also initiated the Marseille Imaging Institute, which has been created in July 2019, where he is currently the Director. The ambition of Marseille Imaging is to lead and coordinate the imaging forces and strengthen the training-research link on the site as well as the attractiveness and socioeconomic development. His research has attracted extensive coverage in the general and more general media: he was interviewed on French television (TV) (TF1), French radio (Radio France, Europe 1, France Inter), and in magazines (Le Point, La Recherche, Libération, Le Figaro), as well as in Physics World, Underwater Times, and New Scientist.

Dr. Enoch is a member of the Editorial Board of the *Journal of Modern Optics*. He has been an Elected Fellow of the European Academy of Sciences in 2019 and a Fellow Member of the Optical Society of America in 2020. He received the Bronze Medal of the CNRS in 2006 and the Aix-Marseille Innovation Award (Researcher category) in 2019. He has also contributed to many conferences, including Metamaterial's 2017 (Scientific and Organization Committees) and International Conference of Electrical, Transport, and Optical Properties on Inhomogeneous Media (ETOPIM)9 (Co-Convenor). He was an Associate Editor of *Optics Express* from 2004 to 2012.